

Research Article

Effects of Annular Combustor Width on the Ethylene-Air Continuous Rotating Detonation

Weijie Fan, Shijie Liu , Jin Zhou, Haoyang Peng, and Siyuan Huang

Science and Technology on Scramjet Laboratory, College of Aerospace Science and Technology, National University of Defense Technology, Changsha, Hunan 410073, China

Correspondence should be addressed to Shijie Liu; liushijie@nudt.edu.cn

Received 13 July 2020; Revised 21 August 2020; Accepted 25 August 2020; Published 14 September 2020

Academic Editor: Jing-Lei Xu

Copyright © 2020 Weijie Fan et al. This is an open access article distributed under the Creative Commons Attribution License, which permits unrestricted use, distribution, and reproduction in any medium, provided the original work is properly cited.

The realization and stable operation of Continuous Rotating Detonation (CRD) in the annular combustor fueled by hydrocarbon-air are still challenging. For further investigation of this issue, a series of ethylene-air CRD tests with the variation of combustor width is conducted, and the effects of combustor width are well analyzed based on high-frequency pressure and high-speed photograph images. The results show that the combustor width plays a significant role in the realization and sustainability of the ethylene-air CRD. In this paper, the critical combustor width for the CRD realization and stable single wave are 20 mm and 25 mm, respectively. In wide combustors, the backward-facing step at the combustor forepart makes the main flow slow down, and thus, the mixing quality is promoted. Besides, the pilot flame at the recirculation zone contributes to sustaining the CRD wave. As the width increases, the propagation mode changes from counter-rotating two-wave mode to single wave mode with higher propagation velocity and stability. The highest propagation velocity reaches 1325.56 m/s in the 40 mm wide combustor, accounting for 71.51% of the corresponding Chapman-Jouguet velocity. Despite large combustor volume, high combustor pressure is obtained in detonation combustion mode indicating that a better propulsive performance could be achieved by CRD.

1. Introduction

Conventional aerospace propulsive systems, such as rocket engine, turbojet engine, ramjet, and scramjet, generally work in the form of isobaric combustion. Isobaric combustion has been deeply studied, and its propulsive performance has gradually approached the upper limit of the theoretical value. Compared with isobaric combustion, detonation is a promising combustion form that may achieve a better propulsive performance, because of its higher thermodynamic efficiency and faster heat release rate [1, 2]. Generally, detonation engines can be classified as Pulse Detonation Engine (PDE) [3], Oblique Detonation Engine (ODE) [4], and Continuous Rotating Detonation Engine (CRDE) [5, 6]. Additionally, CRDEs do not require repeated ignition. Therefore, CRDE has attracted great attention in the propulsion research field [7–13]. In CRDE, fuel and oxidizer are usually injected at the head of the annular combustor, and the CRD wave propagates circumferentially consuming the combustible propel-

lant. Then, the combustion products exhaust at the other end of the combustor and produce a stable thrust.

In 1959, stationary detonation was first proposed by Voitsekhovskii, and the author realized $C_2H_2-O_2$ CRD in a disk-shaped experimental device [14]. Nicholls et al. [15] experimentally investigated the feasibility of CRDE and realized short CRD in an annular combustor. However, there were only a few researches on CRDE for decades. In the past decade, CRDE gradually came under the spotlight again and aroused great interests of many researchers. Extensive CRD investigations fueled by hydrogen were carried out due to the low realization difficulty. And the operation processes of CRDE were studied, including initiation [16–18], propagation characteristics [5, 6, 19], and propulsive performance [12, 20].

Although hydrogen CRD can be easily obtained in a wide operating range, hydrocarbon fuel, especially kerosene [21–23], is considered as a more reliable and affordable option for engineering application. As a main component of kerosene

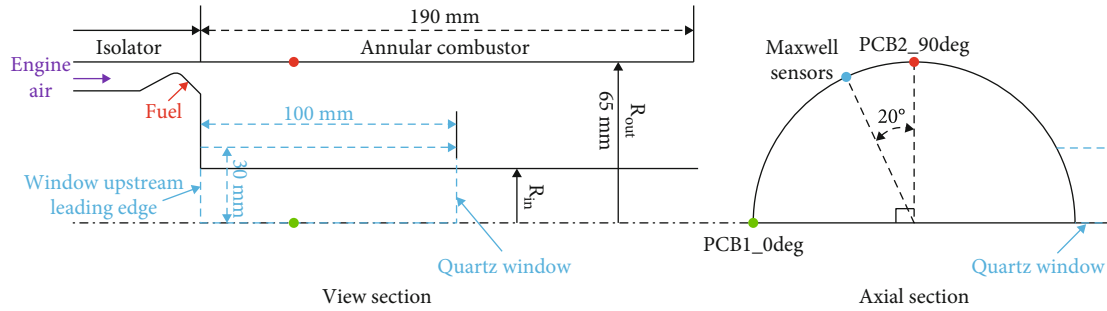


FIGURE 1: Schematic diagrams of test section and sensor installation.

pyrolysis products, ethylene is one of the real fuels for CRDE with regenerative cooling technology. Researches on ethylene CRD can provide a basic understanding of hydrocarbon CRD. However, stable operation of ethylene-air CRD with a low velocity deficit in the annular combustor is still an unsolved problem. Cho et al. [24] carried out a series of experiments on ethylene-air CRD in the optically accessible annular combustor. The propellant was nearly stoichiometric while the propagation velocity was only 994 ± 43 m/s in counter-rotating two-wave mode. St. George et al. [25] performed ethylene-air CRD experiment in the 7.6 mm wide annular combustor. However, the CRD wave propagated at the highest velocity of 850 m/s with severe instability and a great velocity deficit. Andrus et al. [26] experimentally studied ethylene-air CRD using both nonpremixed and premixed supplying schemes in the 23 mm wide annular combustor. The CRD wave propagation velocity was close to CEA predicted sound speed around 1000 m/s, which was significantly lower than the C-J velocity. Wilhite et al. [27] conducted ethylene-air CRD experiment in the annular combustor with a 13.1 mm wide channel. The CRD wave propagated in the velocity close to isobaric sound speed, and a great velocity deficit occurred. The detonation of hydrocarbon in the annular combustor needs further study.

For now, new combustor configurations of CRDE are proposed to enhance hydrocarbon CRD, including hollow combustor and cavity-based annular combustor. Peng et al. [28] performed the ethylene CRD in the optical accessible racetrack-like combustor with oxygen-enriched air. The CRD wave propagated in single wave mode with relatively high velocity at 1647.92 m/s. Furthermore, Peng et al. [29] achieved ethylene-air CRD with large operating range and low velocity deficit in the hollow combustor with a Laval nozzle. The highest propagation velocity reached 1915.4 m/s in single wave mode. Anand et al. [30] successfully obtained ethylene-air CRD in the hollow combustor, and the wave propagation velocity accounted for 95% of the ideal C-J detonation velocity. Wang et al. [31] also realized ethylene-air CRD in the hollow combustor with an outer diameter of 100 mm. The detonation velocities were between 1256 and 1653 m/s, most of which were above 80% of the C-J detonation velocity. Hollow combustor indeed conduces to the realization of ethylene CRD. However, inefficient propulsive performance of CRD in the hollow combustor was reported [20, 32]. Due to low pressure in the combustor, the specific impulses were below 80% of the ideal expansion value in

the study of Kawasaki et al. [32]. Cavity-based annular combustor is a new configuration proposed by the group of Peng [33–35]. By applying the cavity to annular combustor, the CRD wave propagation velocity could reach 1228.68 m/s around stoichiometric equivalence ratio (ER) accounting for 67.4% of the corresponding C-J velocity. The recirculation zone of the cavity had great effects on the CRD and could change the CRD propagation mode. It is suggested that the proper combustor is indeed conducive to the self-sustaining of CRD wave, and which combustor geometry is the main key factor to stable CRD operation deserves further investigation.

Hollow combustor can be considered as a special configuration of annular combustor, in which the inner cylinder is removed and the combustor width enlarge significantly. Although the combustor width was considered to play a key role in the hydrocarbon CRD [36], the realization and stable operation of the hydrocarbon CRD in the enlarged annular combustor have not been achieved. Thus, the transition from annular combustor to hollow combustor on the variation of combustor width deserves to be further investigated. In this paper, a series of tests fueled by ethylene-air have been experimentally conducted. The operating range and propagation characteristics are summarized. Three combustion modes are analyzed through the time-averaged and high-frequency pressure results. In addition, the flowfields are captured by high-speed photograph camera. This study will reveal the effects of annular combustor width on the ethylene-air CRD and improve the combustor design theory of CRD fueled by hydrocarbon fuels.

2. Experimental System

The schematic of the annular combustor is shown in Figure 1. The length and the outer diameter of the annular combustor are 230 mm and 130 mm, respectively. The combustion products are directly discharged into the atmosphere at the exit. To investigate the effects of width, the inner diameters of the annular combustor decrease from 100 mm to 50 mm at the interval of 10 mm in this paper. So that six widths of the annular combustor vary from 15 mm to 40 mm at the interval of 5 mm, labeled as W-15, 20, 25, 30, 35, and 40. Ambient-temperature air is supplied through an annular convergent-divergent slit with a 1.2 mm wide throat. And ambient-temperature ethylene is injected into the combustor through 120 injectors, which are uniformly

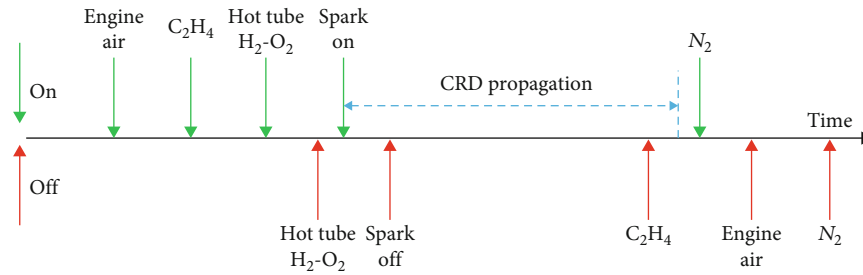


FIGURE 2: Time sequence of experimental tests.

distributed over the inner circumference with a diameter of 0.5 mm. Stable mass flow is provided by sonic injectors installed in the feeding lines. The accurate mass flow rate is measured by turbine flow meters, whose measurement error is within 1%.

The time-averaged and high-frequency pressure measurements are adopted in this paper, which were verified in previous studies [33–35]. The time-averaged pressures in the combustor are acquired by piezo-resistance sensors (Maxwell, Model MPM480). The measurement frequency of the sensor is 500 Hz, and its error is within 0.5% full scale (FS). Eleven sensors (P1-P11) are uniformly installed along the axial direction with an interval of 20 mm, and the first sensor P1 is located at the throat of the air injection slit. The high-frequency pressures in the combustor are obtained by two piezoelectric sensors (PCB113B24) with the NI measure system. The NI measure system samples the dynamic pressure with a $0.5 \mu\text{s}$ interval. The PCB sensor has a resolution of 35 Pa and a rise time of less than $2.0 \mu\text{s}$ with a measurement range of 6895 Pa. The two PCB sensors are installed in the same axial cross-section, which is 40 mm downflow away from the throat of the air injection slit. There is a circumferential angle of 90° between the two PCB sensors. The details of the sensor installation are also displayed in Figure 1.

The time sequence used in this paper is shown in Figure 2. The air and ethylene are turned on in sequence. Then, the hydrogen and oxygen are injected into the hot tube. Afterwards, the mixture of hydrogen and oxygen is ignited by a spark plug in the hot tube. Later, the CRD wave is initiated by the detonation wave generated in the hot tube. After successful initiation, the CRD wave can propagate more than 300 ms. Then, the supply of ethylene is turned off and the combustion is extinguished by nitrogen. Finally, the supply of air and nitrogen is turned off, and one experiment terminates.

For better understanding of the flowfields, the high-speed photograph images are captured by the Photron Fast Camera SA-X. The optical observation quartz window is attached in the outer body of the combustor, as displayed in Figure 1. The window is in a rectangle shape with a size of $100 \text{ mm} \times 60 \text{ mm}$. The window upstream leading edge is in the same axial cross-section with the entrance of the combustor. In this paper, high-speed photograph images are taken at 45000 frames per second (fps). And the resolution and exposure time are 416×640 pixels and $1/65842 \text{ s}$, respectively.

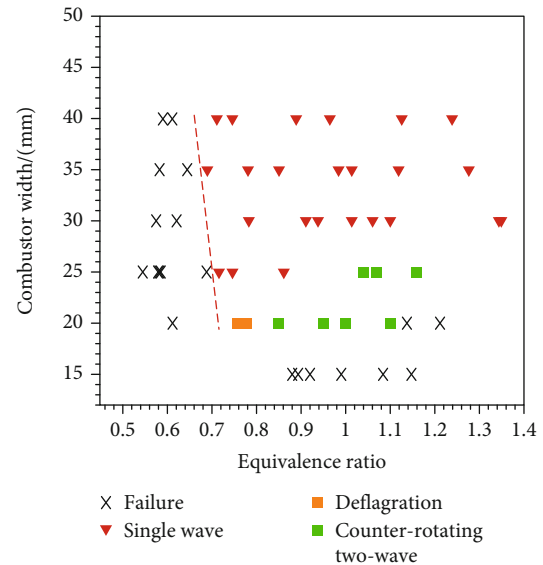


FIGURE 3: Operating range.

3. Results and Discussion

A series of tests have been conducted by changing ER and combustor width. The air mass flow rate is controlled in a relatively stable range of $750 \pm 10 \text{ g/s}$ in all tests. According to the pressure measurement results and optical observation, the operating range and CRD propagation characteristics are analyzed in detail. The effects of combustor widths are also summarized.

3.1. Operating Range and Combustion Mode. The operating range of all the tests with six combustor widths is shown in Figure 3. All the successful CRD cases can be classified into three modes, i.e., single wave mode, counter-rotating two-wave mode, and deflagration. In failure tests, the combustion cannot self-sustain in the combustor before the close of fuel supply. There is a lean ER limit for each combustor configuration. When the ER is lower than the limit value, the stable combustion (including deflagration and detonation) fails. As the combustor width increases, the lean ER limit decreases. This indicates a wider operating range for CRD with larger combustor width. Due to low chemical activity and large detonation cell size, stable single wave fueled by ethylene-air was hardly achieved in the annular combustor with small width [24–27]. However, the CRD waves propagate in single wave

TABLE 1: The typical experimental tests.

Test	Width/(mm)	$\dot{m}_{air}/(g/s)$	ER	Propagation mode	$\bar{f}/(kHz)$
#1	40	756	0.96	Single wave mode	3.19
#2	25	745	1.07	Counter-rotating two-wave mode	2.48
#3	20	744	0.76	Deflagration	—

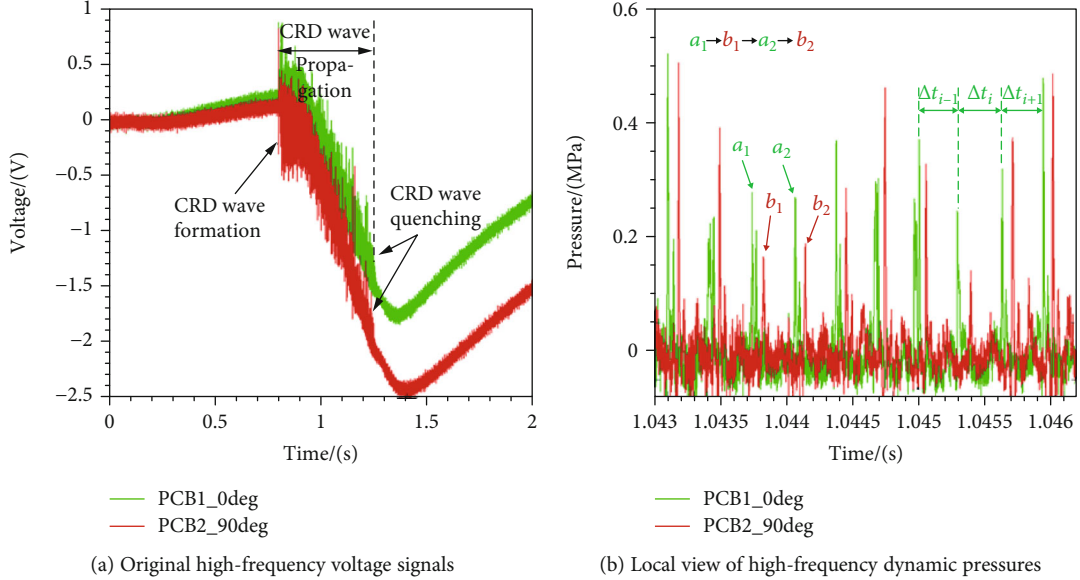


FIGURE 4: High-frequency pressure results of Test #1.

mode in all the successful tests when the width is in the range of 30-40 mm. There is a deep backward-facing step at the combustor forepart when the combustor width is large. A recirculation zone is formed in that area, and the main flow slows down due to the rapid increase of combustor cross-sectional area. Thus, ethylene and air have more time to get mixed, which can effectively promote the mixing quality. Due to the entrained propellant, deflagration also happens at the recirculation zone working as pilot flame [34]. Deflagration flame acts as ignition source with the effects of turbulence and high temperature, which is conducive to the realization and stable propagation of CRD wave. All these factors contribute to stable single wave propagation in the combustors with wide annulus.

For W-25 tests, single wave is also obtained on lean ER and the lean ER limit is about 0.7. It can be found that 25 mm is the critical width value to obtain single wave. And counter-rotating two-wave mode is observed in rich ER. The CRD waves may quench if the intensity of CRD front is not strong enough. Counter-rotating two-wave mode is an effective way to accelerate and enhance heat release. The periodic collision of CRD waves contributes to a rapid release of energy, which helps the CRD waves self-sustain. For W-20 tests, single wave cannot be achieved. The combustion mode changes from deflagration to counter-rotating two-wave mode with ER increasing. Deflagration is a conventional isobaric combustion mode without high-pressure CRD wave. As the ER gradually increases, the chemical activity of ethylene-air mixture gets improved. As a result, CRD wave

can self-sustain in counter-rotating two-wave mode. However, there is a rich ER limit at about 1.1. So that the CRD wave can only be obtained in a small operating range when the width is 20 mm. With the smallest width of 15 mm, in this paper, all the tests fail to obtain CRD. As the width decreases, the backward-facing step at the combustor forepart gets shallow. The propellant flows downstream with high axial velocity after the convergent-divergent slit. Thus, the fuel cannot fully mix with air in short residence time resulting in poor mixing quality. Additionally, the volume of recirculation zone also decreases as the combustor width decreases. The effects of deflagration working as pilot flame at that zone get weakened. As a result, combustion mode transforms in W-20 and W-25 tests. For W-15, there is no backward-facing step at the entrance of the combustor and the recirculation zone disappears. The velocity of the main flow increases distinctly without significant recirculation zone, and no pilot flame can sustain in the combustor forepart. The enhanced combustor organization is destroyed, and thus, the CRD wave cannot be successfully obtained in the 15 mm wide combustor. Above all, greater combustor width is beneficial for easier initiation and wider operating range of CRD wave, due to better mixing quality and the pilot flame at the recirculation zone.

3.2. Propagation Characteristics. Table 1 lists the typical experimental tests and the corresponding conditions. The combustion modes and pressure characteristics in combustor are analyzed in detail. It is worth noting that \bar{f} is the averaged propagation frequency of the CRD wave.

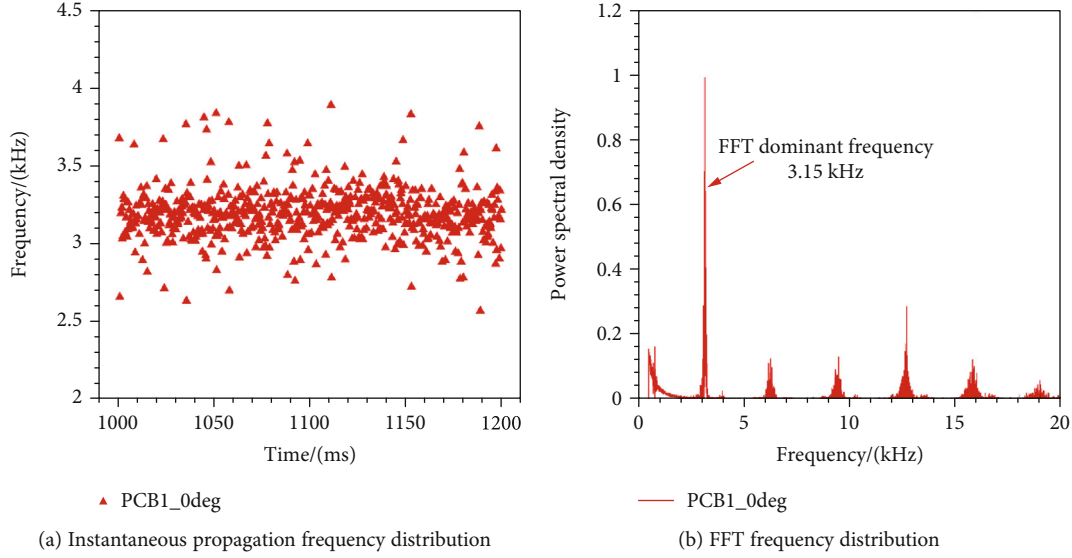


FIGURE 5: Propagation frequency of Test #1.

3.2.1. Single Wave Mode. Figure 4 shows the high-frequency pressure results of Test #1, including the original high-frequency voltage signals and local view of high-frequency dynamic pressures. Resulted from the high propagation frequency and great heat release of CRD wave, the PCB sensors do not have enough time to get recovered. The negligible drift accumulates in the CRD wave propagation duration. Thus, the voltage represents a decline, which is called thermal drift. It can also be seen that the CRD wave is formed at about 0.8 s generating the evident voltage rise. And the detonation quenches at about 1.25 s with the vanishment of evident voltage rise. The supply of ethylene is shut off at 1.2 s while the residual fuel in the pipeline and fuel plenum still supports the CRD wave to rotate for a duration until 1.25 s. The CRD wave can continuously propagate for about 0.45 s. The high-pass filtering process is applied to eliminate the thermal drift and obtain the high-frequency pressure signals, as shown in Figure 4(b). When the CRD wave passes the PCB, the high pressure of CRD wave is captured. It is obvious that the peak pressures recorded by the two PCB sensors occur periodically, namely, “ $a_1 \rightarrow b_1 \rightarrow a_2 \rightarrow b_2$.” And the peak pressures are in the range of 0.1 MPa to 0.5 MPa.

The instantaneous rotating frequency can be calculated by $f_i = 1/\Delta t_i$, where f_i is the instantaneous rotating frequency and Δt_i is the time interval of two peak pressures in sequence recorded by the same PCB sensor, as marked in Figure 4(b). The averaged propagation frequency \bar{f} can be calculated by $\bar{f} = (\sum_{i=1}^N f_i)/N$, where N is the number of rotating cycles in the stable propagation duration. The instantaneous frequency distribution and Fast Fourier Transformation (FFT) frequency distribution of Test #1 are illustrated in Figure 5. The averaged propagation frequency and FFT dominant frequency of Test #1 are, respectively, calculated as 3.19 kHz and 3.15 kHz. The two calculation methods of propagation frequency show a good coincidence with the relative error of 1.25%. The averaged propagation velocity \bar{v} can be calculated as $\bar{v} = \pi D_{\text{out}} \bar{f}$, where D_{out} represents the outer diameter of the

combustor, i.e., 130 mm. The averaged propagation velocity of Test #1 is calculated as 1304.41 m/s accounting for 71.98% of the corresponding C-J velocity. The propagation performance significantly exceeds other investigations of ethylene-air CRD in the annular combustor. Considering there may be multiple CRD waves in corotating mode, the number of CRD wave should be confirmed further. It can be confirmed as following Eqs. (1)–(3), where n is the number of CRD wavefront and θ is the circumferential angle of PCB1 and PCB2, namely, $\pi/2$. Obviously, t_{a1b1}/t_{a1a2} is approximately 1/4. So, n is confirmed as 1, and the CRD wave indeed propagates in single wave mode.

$$t_{a1a2} = (\pi D_{\text{out}} \bar{f}) \times \frac{1}{n}, \quad (1)$$

$$t_{a1b1} = (\pi D_{\text{out}} \bar{f}) \times \frac{\theta}{2\pi}, \quad (2)$$

$$n = \frac{2\pi}{\theta} \times \frac{t_{a1b1}}{t_{a1a2}}. \quad (3)$$

The sequential high-speed photography images of Test #1 are displayed in Figure 6. The front of CRD is quite bright due to the great chemiluminescence, which is marked by the red solid line. Obviously, the CRD wave propagates from top to bottom in Frame-1 to 4, and the propagation direction is marked by the red arrow. In Frame-5 and 6, the CRD wave propagates on the other side of the combustor, and thus, it cannot be observed in the quartz window. Due to the deep recirculation zone, much propellant is entrained into the zone. The flame holding ability of the recirculation zone and the effects of pilot flame at that zone are both enhanced. As a result, the detonation combustion flame is concentrated near the forepart of the combustor with great luminance, indicating that the CRD wave can stably sustain with strong intensity.

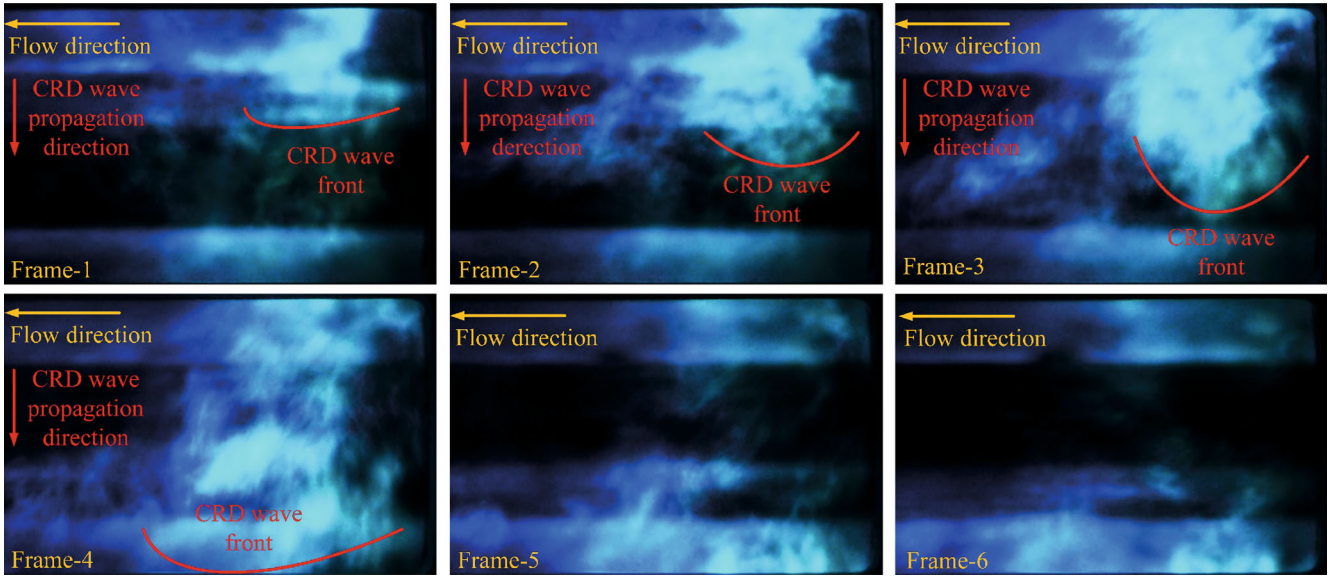


FIGURE 6: High-speed photography images of Test #1.

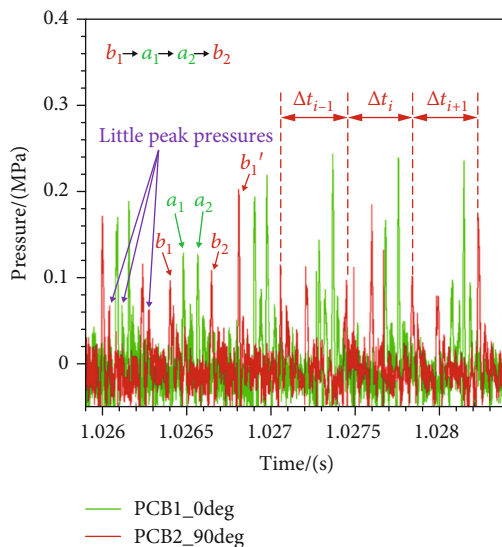


FIGURE 7: Local view of high-frequency dynamic pressures of Test #2.

3.2.2. Counter-Rotating Two-Wave Mode. The local view of high-frequency dynamic pressures of Test #2 is illustrated in Figure 7. It is clear that the pressures fluctuate in “ $b_1 \rightarrow a_1 \rightarrow a_2 \rightarrow b_2$ ” repetition. It indicates that CRD waves propagate in typical counter-rotating two-wave mode. Inferred from the PCB sensor arrangement and peak pressure sequence, a collision is considered to occur between the inferior arc of the circumference segmented by the two PCB sensors. And the collision location is closer to PCB1, since peak pressure a_1 and a_2 are between b_1 and b_2 . For better understanding of the counter-rotating two-wave propagation mode, a schematic view is shown in Figure 8. The detonation wave M rotates clockwise while N rotates anticlockwise. They collide at P_1 which is out of the quartz window view. After the collision, the detonation waves evolve

into the transmitted shock waves. Later, the transmitted shock waves are accelerated into the detonation waves M_1 and N_1 . Then, N_1 passes PCB2 and M_1 passes PCB1 in sequence generating peak pressures b_1 and a_1 , respectively. After a while, M_1 and N_1 collide at P_2 which is closer to PCB1. Similarly, new detonation waves M_2 and N_2 are generated after the collision. N_2 passes PCB1 and M_2 passes PCB2 in sequence generating peak pressures a_2 and b_2 , respectively. Thus, the peak pressures repeat in regular oscillations “ $b_1 \rightarrow a_1 \rightarrow a_2 \rightarrow b_2$.” The high-speed photography images of counter-rotating two-wave mode in Test #2 are shown in Figure 9. The CRD wave M propagates from top to bottom. Then, it collides with CRD wave N out of the quartz window view. After the collision, transmitted shock waves evolve into CRD waves again and the waves rotate in the original direction. Therefore, CRD wave N_1 propagates from bottom to top, seen in Frame-7 to 12. Due to the shallow recirculation zone in the 25 mm wide combustor, the flame holding ability of the zone and effects of pilot flame at the zone are both weakened. So that the flame in Test #2 is dimmer than that of Test #1, indicating the combustion intensity of counter-rotating two-wave mode is lower than that of single wave mode.

Since there are two waves propagating in counter-rotating direction, the propagation period definition is different from that of single wave mode. As Figure 7 shows, the time of the complete period is the interval of peak pressures b_1 - b_1' rather than b_1 - b_2 . After high-pass filtering processing and FFT processing, the instantaneous propagation frequency and FFT frequency distribution of Test #2 are shown in Figure 10. Its averaged propagation frequency and FFT dominant frequency are, respectively, 2.48 kHz and 2.50 kHz, which are in good accordance. Moreover, the peak pressures of counter-rotating two-wave mode are much lower than those of single wave mode. This indicates that the intensity of counter-rotating two-wave mode is weaker than that of single wave mode. Due to the

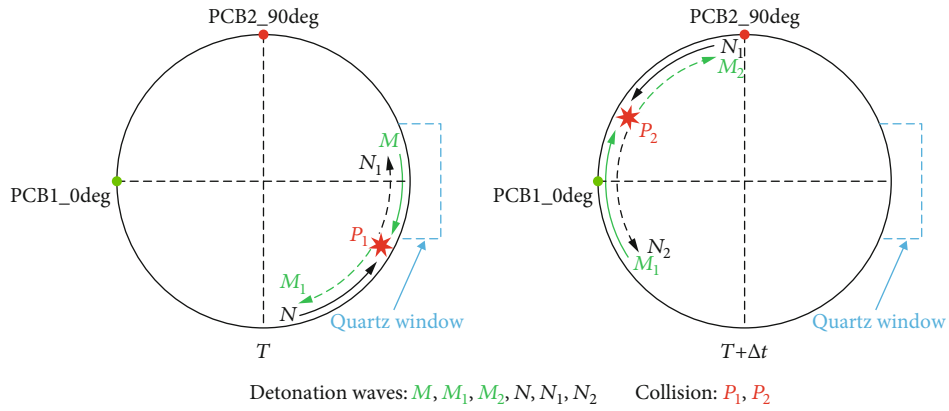


FIGURE 8: Schematic view of counter-rotating two-waves mode.

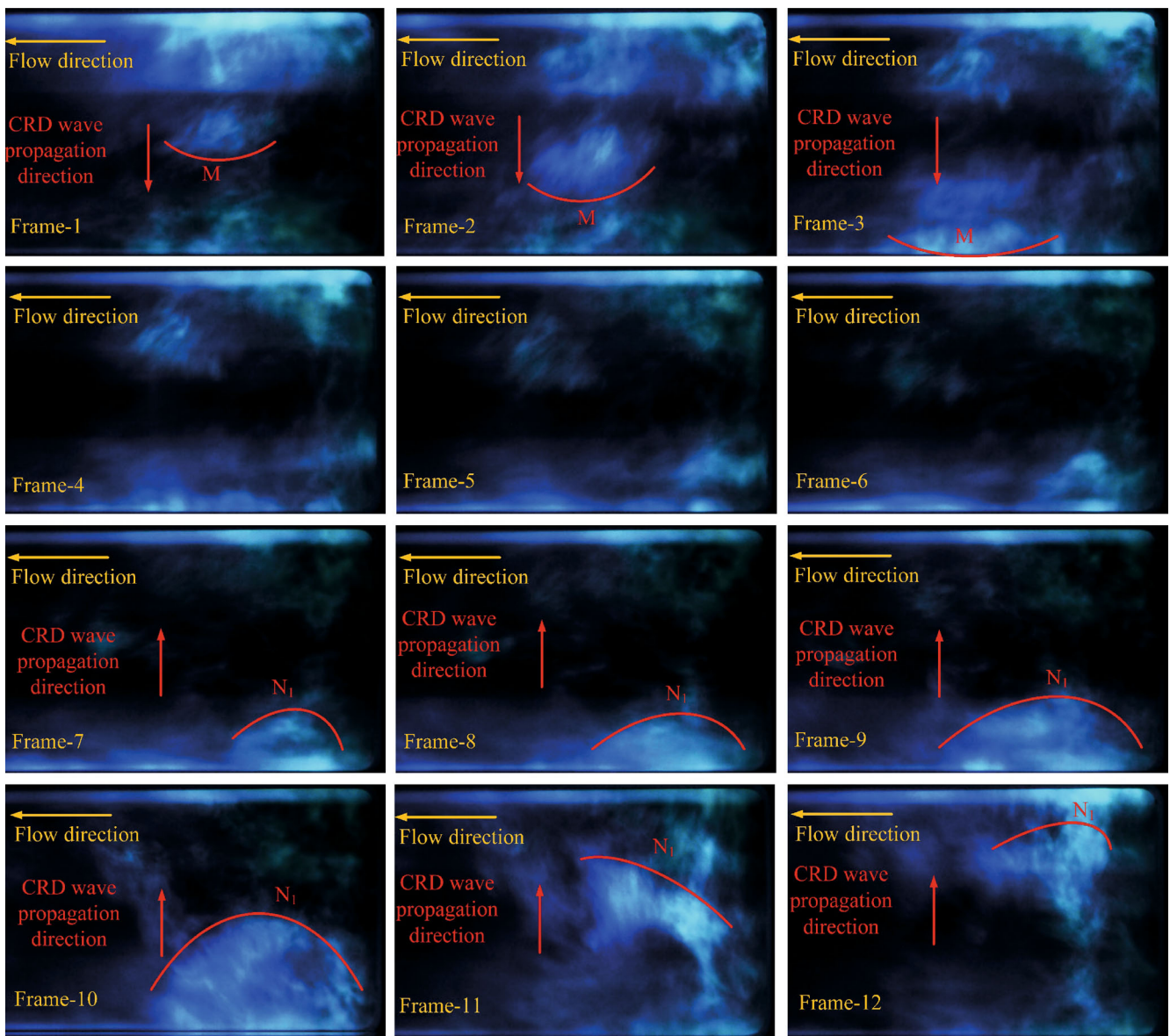


FIGURE 9: High-speed photography images of counter-rotating two-wave mode in Test #2.

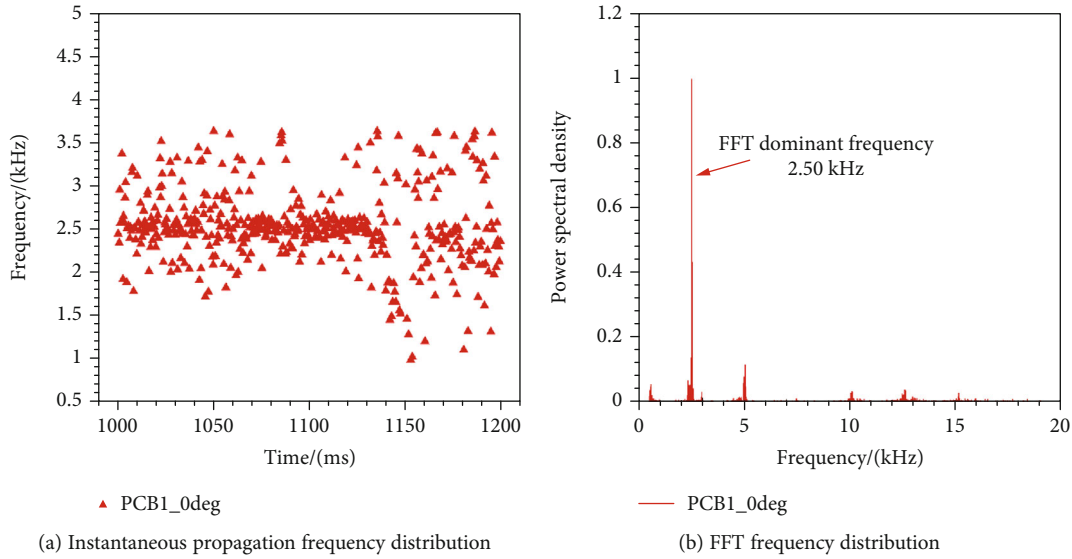


FIGURE 10: Propagation frequency of Test #2.

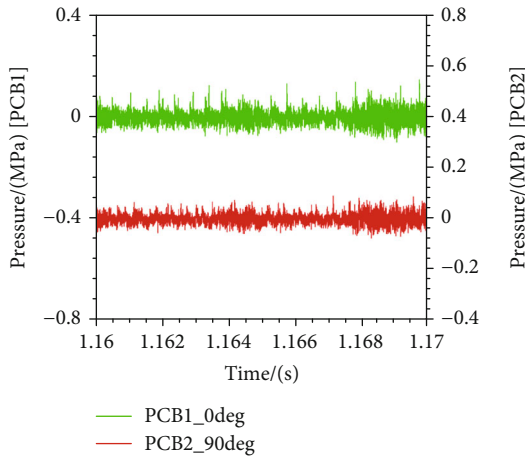


FIGURE 11: Local view of high-frequency dynamic pressures of Test #3.

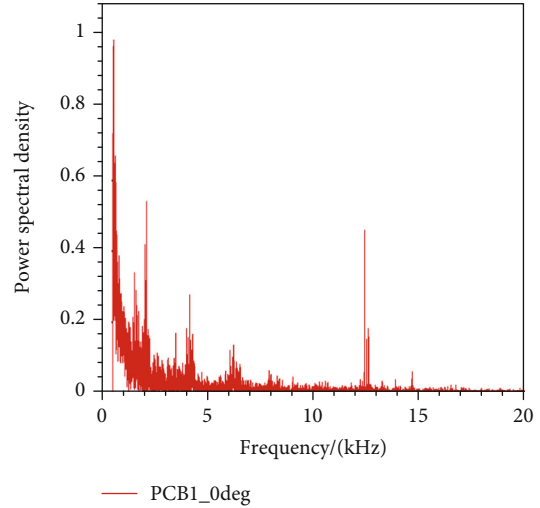


FIGURE 12: FFT frequency distribution of Test #3.

transverse wave effects, there are reflected waves between the inner and outer walls when the annulus width is within a certain range. And this phenomenon was also found and discussed in the investigations of annular combustor [37, 38].

3.2.3. Deflagration. There is no CRD wave propagating circumferentially in the combustor when CRDE works in deflagration mode. The propellant is consumed by traditional isobaric combustion. The local view of high-frequency dynamic pressures of Test #3 is illustrated in Figure 11. The high-frequency pressures fluctuate around 0, and there are no obvious peak pressures or periodic oscillations. These indicate that there is no pressure wave rotating in the combustor. Different from Test #1 and #2, no reliable FFT dominant frequency of Test #3 is obtained in the FFT frequency distribution, as shown in Figure 12. The high-speed photography images of Test #3 are illustrated in Figure 13. The images are quite dim indicating that the intensity of deflagration is much lower than that of CRD modes. The deflagration

mainly occurs near the forepart of the combustor, and the luminance fades away as the main flow moves downstream. There is no distinct combustion flame rotating circumferentially in the combustor, which indicates the CRD wave is not obtained. The axial time-averaged pressures of Test #1-3 recorded by P1-P11 are plotted in Figure 14. The time-averaged pressures of Test #1 are the highest while those in Test #3 are the lowest, indicating that the combustion intensity of single wave mode, counter-rotating two-wave mode, and deflagration decreases in sequence. P1 is located at the throat of the air slit while P2 is located close to the entrance of the combustor. Since there is a backward-facing step at the forepart of the combustor, the cross-sectional area of the combustor increases rapidly so that the time-averaged pressure drops remarkably between P1 and P2. With the same cross-sectional area of the combustor, the pressure increases moderately reaching the first peak at P4 due to the combustion. Resulted from the expansion behind the

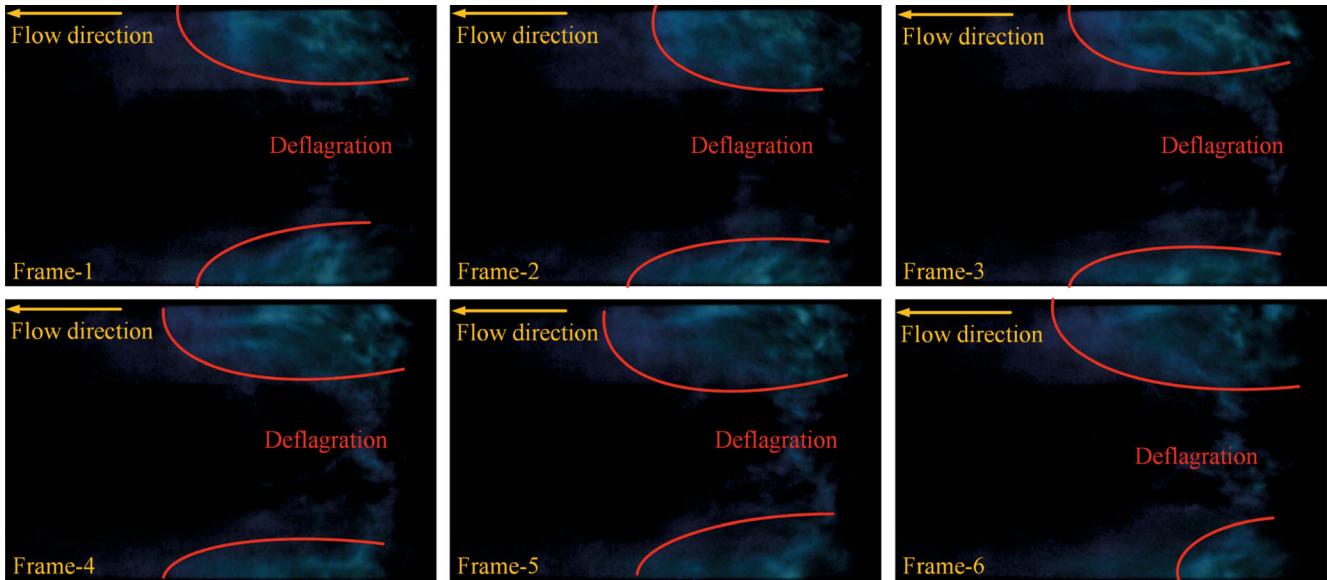


FIGURE 13: High-speed photography images of Test #3.

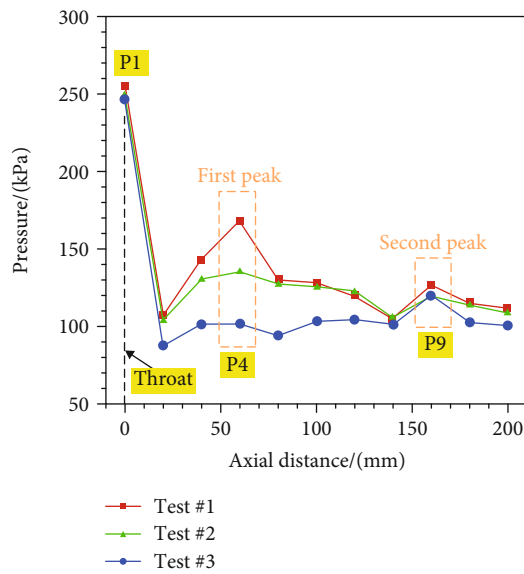


FIGURE 14: Pressure-distance distribution of Test #1-3.

CRD wave, the time-averaged pressure declines between P4 and P8. Affected by the outlet pressure at the exit of the combustor, a second peak of time-averaged pressure occurs at P9.

3.3. Effects of Combustor Width. The effects of combustor width on CRD are summarized in this section. As analyzed above, the highest time-averaged pressure is located within the CRD wave front at the combustor forepart. Thus, the time-averaged pressure of P4 is used to represent the combustor pressure and to estimate the effects of combustor width on the combustion, as shown in Figure 15. In general, the pressure of P4 increases as the combustor width enlarges, mainly due to the difference in combustion mode. The minimal pressure is produced in deflagration mode in combustor W-20. Higher pressure is obtained in counter-rotating two-

wave mode while the highest pressure is achieved in single wave mode. These indicate the CRD mode can obtain higher pressure gain than that of conventional isobaric combustion. The pressure obtained in combustor W-35 is quite close to that in combustor W-40 when ER is lower than 1.2. However, the pressure in combustor W-40 drops dramatically while it keeps stable in combustor W-35 on highly rich ER. It can be inferred that optimal propulsive performance may be achieved in combustor W-35. In addition, P4 pressure in each combustor first increases and then drops as ER increases from lean stage to rich stage. Since high chemical activity of propellant is achieved when the propellant is stoichiometric, high pressures are obtained in that condition.

The effects of combustor width on propagation frequency are shown in Figure 16, and the discussion is only on the detonation modes. The propagation frequency is positively correlated with the combustor width. In combustors W-40, W-35, and W-30, the CRD waves all propagate in single wave mode and the frequency obtained in these combustors is slightly affected by ER variation. In this paper, the highest frequency and velocity of the CRD wave propagation are correspondingly 3.24 kHz and 1325.56 m/s on the ER of 1.12 obtained in combustor W-40. The highest velocity accounts for 71.51% of the corresponding C-J velocity, and it exceeds other investigations [24–27]. With the decrease of combustor width, the counter-rotating two-wave mode is observed in combustors W-25 and W-20. In the 20 mm wide combustor, the frequency is quite low in the range of 2.21–2.32 kHz and the averaged velocity only accounts for 50.31%–52.41% of the corresponding C-J velocity. A great velocity deficit occurs in the 20 mm wide combustor. As mentioned in Section 3.1, when the width decreases, the effects of pilot flame get weakened and the mixing quality gets poor as the backward-facing step shallows. Both the weakened effects of pilot flame and poor mixing quality may lead to the decrease of combustion intensity and propagation velocity. In addition, the collision of waves also contributes to the great velocity deficit.

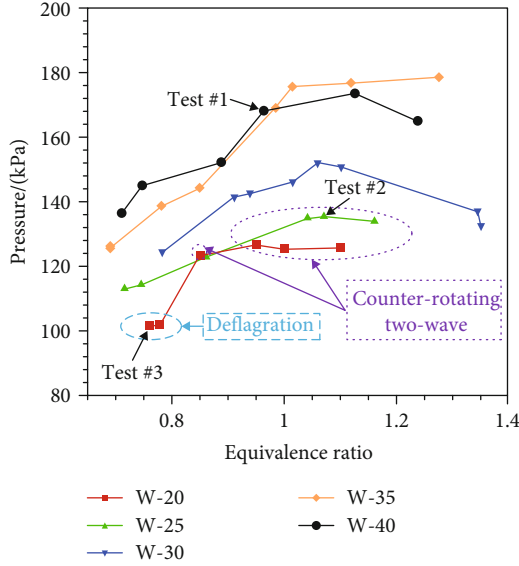


FIGURE 15: Effects of combustor width on P4 pressure in the combustor.

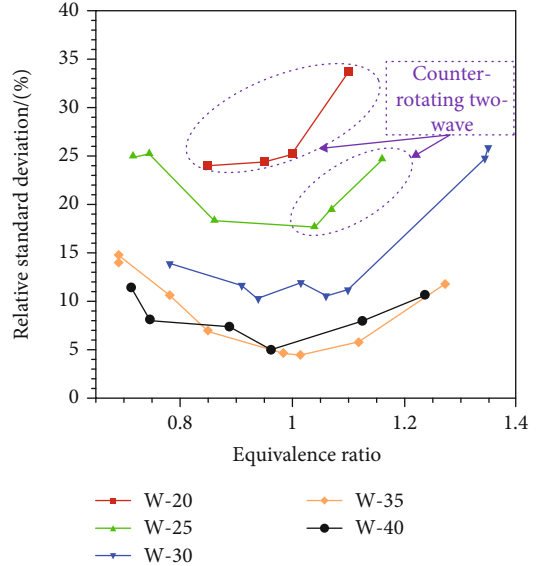


FIGURE 17: Effects of combustor width on propagation stability.

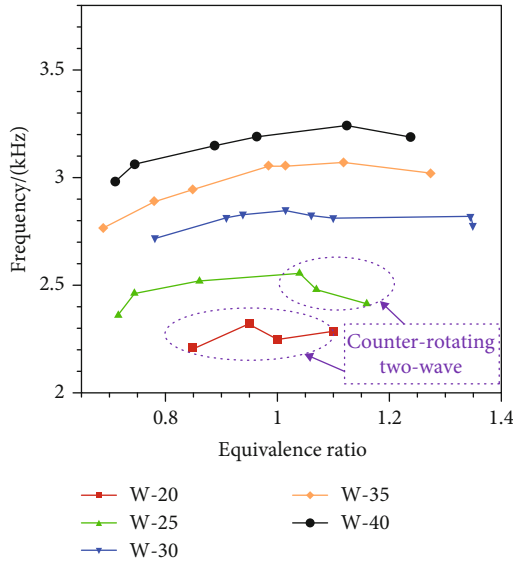


FIGURE 16: Effects of combustor width on propagation frequency.

The effects of combustor width on propagation stability are illustrated in Figure 17. The relative standard deviation of the instantaneous propagation frequency in the propagation duration is used to quantitatively evaluate the stability. The calculation methods are defined as $S = \sqrt{\sum_1^N f_i - \bar{f}} / (N - 1)$ and $\mu = S/f$, where S is standard deviation, N is the number of propagation cycles, and μ is relative standard deviation [29]. The propagation stability is negatively correlated with the combustor width in different CRD propagation modes. Severe instability happens in counter-rotating two-wave mode, and the deviation can be as high as 33.67% in combustor W-20. On the contrary, quite stable CRD wave propagation is obtained in single wave and

the deviations are all below 15% in combustor W-40. It can be inferred that large combustor width contributes to stable propagation of CRD wave. Besides, the deviation goes down first and then rises as ER increases. The minimal value is obtained when ER is about 1.0 in each combustor. When ER is about 1.0, the chemical activity of the propellant is high so that the propellant is easier to get ignited. This is beneficial for stable propagation of the CRD wave. In conclusion, wide combustor and stoichiometric ER both contribute to the stable propagation of the CRD wave.

4. Conclusions

To figure out the effects of combustor width on the ethylene-air CRD in the annular combustor, a series of tests are conducted with ER variation in combustors with different widths. Through the pressure measure results and high-speed photograph images, experiment results have been analyzed in detail. The conclusions are drawn as follows:

- (1) The combustor width has great effects on the realization of ethylene-air CRD, and the critical combustor width for ethylene-air CRD realization is 20 mm in this paper. There is a deep backward-facing step at the combustor forepart when the combustor width is large. Thus, the main flow slows down due to the rapid increase of the combustor cross-sectional area, and the mixing quality is promoted. Besides, the pilot flame at the recirculation zone can greatly conduce to the realization and stable propagation of CRD wave
- (2) The combustor width also has effects on the CRD wave propagation modes, and the critical combustor width to obtain single wave is 25 mm in this paper. As the width increases, the propagation mode changes from counter-rotating two-wave mode to single wave mode. The characteristics of both modes are well

analyzed by high-frequency pressure and high-speed photograph images

- (3) Single wave mode is achieved in wide operating range in wide combustors, and the CRD wave propagates with high frequency in this mode. On the ER of 1.12 in combustor W-40, the highest averaged propagation frequency and velocity are 3.24 kHz and 1325.56 m/s, respectively. The velocity accounts for 71.51% of the corresponding C-J velocity
- (4) When the combustor width is large, high combustor pressure and stable CRD propagation are both obtained. In spite of large combustor volume, higher pressure is acquired by the detonation combustion in wide combustors compared with that of deflagration in combustor W-20. The relative standard deviation of the instantaneous propagation frequency decreases dramatically as the combustor width increases. The deviation can be lower than 15% in single wave mode in combustor W-40. It can be inferred that a better propulsive performance could be approached by the detonation combustion, especially for single wave mode

This paper will provide a deeper understanding of hydrocarbon CRD realization mechanism and enrich the combustor design theory for CRDE.

Data Availability

The data used to support the findings of this study are available from the corresponding author upon request.

Conflicts of Interest

The authors declare there is no conflict of interest regarding the publication of this paper.

Acknowledgments

This work is supported by the National Natural Science Foundation of China through Grant No. (51776220 and 91541103).

References

- [1] F. A. Bykovskii and E. F. Vedernikov, "Self-sustaining pulsating detonation of gas-mixture flow," *Combustion, Explosion, and Shock Waves*, vol. 32, no. 4, pp. 442–448, 1996.
- [2] D. S. Stewart and A. R. Kasimov, "State of detonation stability theory and its application to propulsion," *Journal of Propulsion and Power*, vol. 22, no. 6, pp. 1230–1244, 2006.
- [3] V. F. Nikitin, V. R. Dushin, Y. G. Phylippov, and J. C. Legros, "Pulse detonation engines: technical approaches," *Acta Astronautica*, vol. 64, no. 2-3, pp. 281–287, 2009.
- [4] X. Cai, J. Liang, R. Deiterding, Y. Che, and Z. Lin, "Adaptive mesh refinement based simulations of three-dimensional detonation combustion in supersonic combustible mixtures with a detailed reaction model," *International Journal of Hydrogen Energy*, vol. 41, no. 4, pp. 3222–3239, 2016.
- [5] W. Lin, J. Zhou, S. Liu, Z. Lin, and F. Zhuang, "Experimental study on propagation mode of H₂/air continuously rotating detonation wave," *International Journal of Hydrogen Energy*, vol. 40, no. 4, pp. 1980–1993, 2015.
- [6] V. Anand, A. St. George, R. Driscoll, and E. Gutmark, "Investigation of rotating detonation combustor operation with H₂-air mixtures," *International Journal of Hydrogen Energy*, vol. 41, no. 2, pp. 1281–1292, 2016.
- [7] S. A. Zhdan, "Mathematical model of continuous detonation in an annular combustor with a supersonic flow velocity," *Combustion, Explosion, and Shock Waves*, vol. 44, no. 6, pp. 690–697, 2008.
- [8] M. Hishida, T. Fujiwara, and P. Wolanski, "Fundamentals of rotating detonations," *Shock Waves*, vol. 19, no. 1, pp. 1–10, 2009.
- [9] T. Gaillard, D. Davidenko, and F. Dupoirieux, "Numerical simulation of a rotating detonation with a realistic injector designed for separate supply of gaseous hydrogen and oxygen," *Acta Astronautica*, vol. 141, pp. 64–78, 2017.
- [10] C. A. Nordeen, D. Schwer, F. Schauer, J. Hoke, T. Barber, and B. M. Cetegen, "Role of inlet reactant mixedness on the thermodynamic performance of a rotating detonation engine," *Shock Waves*, vol. 26, no. 4, pp. 417–428, 2016.
- [11] J. Sun, J. Zhou, S. Liu, Z. Lin, and J. Cai, "Effects of injection nozzle exit width on rotating detonation engine," *Acta Astronautica*, vol. 140, pp. 388–401, 2017.
- [12] J. Sun, J. Zhou, S. Liu, Z. Lin, and W. Lin, "Plume flowfield and propulsive performance analysis of a rotating detonation engine," *Aerospace Science and Technology*, vol. 81, pp. 383–393, 2018.
- [13] J. Sun, J. Zhou, S. Liu, and Z. Lin, "Numerical investigation of a rotating detonation engine under premixed/non-premixed conditions," *Acta Astronautica*, vol. 152, pp. 630–638, 2018.
- [14] B. V. Voitsekhovskii, "Stationary detonation," *Doklady Akademii Nauk USSR*, vol. 129, pp. 1254–1256, 1959.
- [15] J. A. Nicholls, R. E. Cullen, and K. W. Ragland, "Feasibility studies of a rotating detonation wave rocket motor," *Journal of Spacecraft and Rockets*, vol. 3, no. 6, pp. 893–898, 1966.
- [16] E. Braun, N. Dunn, and F. Lu, "Testing of a continuous detonation wave engine with swirled injection," in *48th AIAA Aerospace Sciences Meeting Including the New Horizons Forum and Aerospace Exposition*, Orlando, FL, USA, January 2010.
- [17] L. Peng, D. Wang, X. Wu, H. Ma, and C. Yang, "Ignition experiment with automotive spark on rotating detonation engine," *International Journal of Hydrogen Energy*, vol. 40, no. 26, pp. 8465–8474, 2015.
- [18] C. Yang, X. Wu, H. Ma, L. Peng, and J. Gao, "Experimental research on initiation characteristics of a rotating detonation engine," *Experimental Thermal and Fluid Science*, vol. 71, pp. 154–163, 2016.
- [19] S. Liu, W. Liu, Z. Lin, and W. Lin, "Experimental research on the propagation characteristics of continuous rotating detonation wave near the operating boundary," *Combustion Science and Technology*, vol. 187, no. 11, pp. 1790–1804, 2015.
- [20] X. M. Tang, J. P. Wang, and Y. T. Shao, "Three-dimensional numerical investigations of the rotating detonation engine with a hollow combustor," *Combustion and Flame*, vol. 162, no. 4, pp. 997–1008, 2015.
- [21] F. A. Bykovskii, S. A. Zhdan, and E. F. Vedernikov, "Continuous spin detonation of fuel-air mixtures," *Combustion, Explosion and Shock Waves*, vol. 42, no. 4, pp. 463–471, 2006.

- [22] J. Kindracki, "Experimental research on rotating detonation in liquid fuel-gaseous air mixtures," *Aerospace Science and Technology*, vol. 43, pp. 445–453, 2015.
- [23] B. Le Naour, F. H. Falempin, and K. Coulon, "MBDA R&T effort regarding continuous detonation wave engine for propulsion-status in 2016," in *21st AIAA International Space Planes and Hypersonics Technologies Conference*, Xiamen, China, March 2017.
- [24] K. Y. Cho, J. R. Codoni, B. A. Rankin, J. Hoke, and F. Schauer, "High-repetition-rate chemiluminescence imaging of a rotating detonation engine," in *54th AIAA Aerospace Sciences Meeting*, San Diego, CA, USA, January 2016.
- [25] A. C. St. George, R. B. Driscoll, V. Anand, D. E. Munday, and E. J. Gutmark, "Fuel blending as a means to achieve initiation in a rotating detonation engine," in *53rd AIAA Aerospace Sciences Meeting*, Kissimmee, FL, USA, January 2015.
- [26] I. Q. Andrus, M. D. Polanka, P. I. King, F. R. Schauer, and J. L. Hoke, "Experimentation of premixed rotating detonation engine using variable slot feed plenum," *Journal of Propulsion and Power*, vol. 33, no. 6, pp. 1448–1458, 2017.
- [27] J. Wilhite, R. B. Driscoll, A. C. St. George, V. Anand, and E. J. Gutmark, "Investigation of a rotating detonation engine using ethylene-air mixtures," in *54th AIAA Aerospace Sciences Meeting*, San Diego, CA, USA, January 2016.
- [28] H. Peng, W. Liu, and S. Liu, "Ethylene Continuous Rotating Detonation in optically accessible racetrack-like combustor," *Combustion Science and Technology*, vol. 191, no. 4-6, pp. 676–695, 2019.
- [29] H. Peng, W. Liu, S. Liu, and H. Zhang, "Experimental investigations on ethylene-air continuous rotating detonation wave in the hollow chamber with Laval nozzle," *Acta Astronautica*, vol. 151, pp. 137–145, 2018.
- [30] V. Anand, A. St. George, C. Farbos de Luzan, and E. Gutmark, "Rotating detonation wave mechanics through ethylene-air mixtures in hollow combustors, and implications to high frequency combustion instabilities," *Experimental Thermal and Fluid Science*, vol. 92, pp. 314–325, 2018.
- [31] Y. Wang, J. le, C. Wang, and Y. Zheng, "A non-premixed rotating detonation engine using ethylene and air," *Applied Thermal Engineering*, vol. 137, pp. 749–757, 2018.
- [32] A. Kawasaki, T. Inakawa, J. Kasahara et al., "Critical condition of inner cylinder radius for sustaining rotating detonation waves in rotating detonation engine thruster," *Proceedings of the Combustion Institute*, vol. 37, no. 3, pp. 3461–3469, 2019.
- [33] H. Peng, W. D. Liu, S. Liu, and H. L. Zhang, "The effect of cavity on ethylene-air continuous rotating detonation in the annular combustor," *International Journal of Hydrogen Energy*, vol. 44, no. 26, pp. 14032–14043, 2019.
- [34] S.-J. Liu, H. Y. Peng, W. D. Liu, and H. L. Zhang, "Effects of cavity depth on the ethylene-air continuous rotating detonation," *Acta Astronautica*, vol. 166, pp. 1–10, 2020.
- [35] H. Y. Peng, W. D. Liu, S. J. Liu, and H. L. Zhang, "Effects of cavity location on ethylene-air continuous rotating detonation in a cavity-based annular combustor," *Combustion Science and Technology*, vol. 192, pp. 1–22, 2020.
- [36] F. A. Bykovskii, S. A. Zhdan, and E. F. Vedernikov, "Continuous spin detonations," *Journal of Propulsion and Power*, vol. 22, no. 6, pp. 1204–1216, 2006.
- [37] R. Zhou and J.-P. Wang, "Numerical investigation of shock wave reflections near the head ends of rotating detonation engines," *Shock Waves*, vol. 23, no. 5, pp. 461–472, 2013.
- [38] H. Zhang, W. Liu, and S. Liu, "Effects of inner cylinder length on H₂/air rotating detonation," *International Journal of Hydrogen Energy*, vol. 41, no. 30, pp. 13281–13293, 2016.